Materials Advances

ROYAL SOCIETY OF CHEMISTRY

PAPER

View Article Online
View Journal | View Issue

Cite this: *Mater. Adv.*, 2026, 7, 6254

Self-healable bio-based solid polymer electrolytes incorporating ionic liquids for safer lithium–ion batteries

Kaushiki Ahuja,[a] Shitanshu Pratap Singh,[b] Pratiksha Joshi,[c] Mahendra Singh Lodhi,[c] Rajendra Kumar Singh*[b] and Sravendra Rana*[a]

Self-healable polymeric electrolytes are crucial for ensuring the durability, safety and sustainability of lithium–ion batteries. Herein, we report advances in the design of bio-derived, self-healable solid polymer electrolytes that overcome three well-entrenched limitations – good self-healing behaviour, limited ionic mobility, and a narrow electrochemical window. Using a blend polymeric composition of polyethylene glycol (PEG) and bio-based methyl cellulose (MC) consisting of a dynamic disulfide moiety (covalent adaptive network) and imidazolium-based ionic liquids (EMIM-TFSI, EMIM-Br, and EMIM-Ac), we present a variety of self-healable polymer electrolytes. Synergistic improvements in sustainability, flexibility, ion mobility and potential window by adding different ionic liquids were studied and demonstrated by physicochemical and electrochemical characterization, including FTIR, XRD, DSC, TGA, stress–strain analysis, SEM, ionic conductivity, dielectric study, electrochemical stability window (ESW), and lithium transference number. The prepared self-healable electrolytes possess good ionic conductivity (10^{-3} S cm^{-1}) at higher temperature, a good permittivity value with respect to frequency, a wide electrochemical stability window (>5.5 V), and exceptional scratch-healing efficiency (due to reversible disulfide exchange networks). The integrated self-healing mechanism and superior electrochemical properties validate the potential of the developed self-healable polymer electrolytes as robust candidates for durable solid-state lithium–ion batteries.

Received 16th January 2026,
Accepted 5th May 2026

DOI: 10.1039/d6ma00073h

rsc.li/materials-advances

1. Introduction

Lithium-ion batteries play a significant role in today's world, influencing various sectors from consumer electronics to electric vehicles, attributed to their advantages, including high cell voltage, specific capacity and excellent cycling stability. Despite their dominance, Li-ion batteries present various challenges due to the use of conventional organic carbonate-based electrolytes in these batteries, which struggle with leakage due to their fluid and highly flammable natures.[1] Additionally, the uneven deposition of Li ions at the anode surface during the charging–discharging process[2] promotes the formation of dendrites, which causes a short-circuit in batteries.[3] To resolve these issues, researchers are investigating solid-state polymer electrolytes (SPE), which exhibit mechanical stability and ionic conductivity, as well as lowering the risk of thermal runaway while boosting mechanical flexibility during battery operation.[4] Despite their various advantages, the utilization of gel/solid state polymer electrolytes faces challenges under external stresses, *e.g.*, during stretching, bending, and folding, causing damage to the electrolyte, which further deteriorates the performance of the battery by losing the contact between the electrode and electrolyte interface.[5] Thus, self-healing polymers have garnered considerable attention in the field of battery materials, as they have the potential to address the breakage problem, thereby increasing their longevity, dependability, and sustainability.[6] Electrolytes having self-healing capabilities reduce the chances of short-circuit in lithium battery electrodes, thus lowering the risk of thermal runaway.[7] In addition, the non-flammable nature of SPEs may reduce the possibility of LIB combustion and explosion.

Innovative materials with extrinsic or intrinsic healing properties have been developed by encapsulating reactive healing agents in material matrices or crosslinking components through reversible noncovalent interactions,[8] *e.g.*, hydrogen bonding, ion–dipole interaction,[9] ion–ion interaction, π–π stacking, host–guest interaction, *etc.*,[10] as well as dynamic

[a] *School of Advanced Engineering, UPES, Energy Acres, Bidholi, Dehradun, Uttarakhand, 248007, India. E-mail: srana@ddn.upes.ac.in*
[b] *Ionic Liquid and Solid-State Ionics Lab, Department of Physics, Institute of Science, Banaras Hindu University, Varanasi, Uttar Pradesh, 221005, India. E-mail: rajendrasingh.bhu@gmail.com*
[c] *G.B. Pant National Institute of Himalayan Environment, Almora, Uttarakhand, 263643, India*

covalent connections like Diels–Alder reaction,[11] disulfide exchange,[12] trans-esterification,[13] imine exchange, and boric ester linkages.[14] As intrinsic self-healable materials demonstrate several healing cycles, they are preferable to extrinsic self-healing/healable materials since they rely on the leakage and consumption of healing chemicals after a crack.[15] Despite these advantages, self-healable polymers have not been much explored in Li-batteries due to their low ionic conductivity and less flexibility.[16] Thus, it would be beneficial to design novel self-healing electrolytes with flexible nature and moderate ionic conductivity (10^{-3} to 10^{-4} S cm^{-1}),[17] as well as high mechanical stability, to mitigate the growth of lithium dendrites and to achieve a wide electrochemical stability window.[18] Various strategies have been reported to increase the ionic conductivity of electrolytes, *via* copolymer electrolyte synthesis, and/or the addition of plasticizers and fillers, which disrupts the crystallization of the polymer and leads to an increase in the ionic conductivity.[19]

Among various plasticizers, ionic liquids (ILs), commonly known as molten salts, are good additives for electrolytes owing to their non-flammable nature, high ionic conductivity, thermal stability, wide electrochemical window, and low toxicity.[3] The addition of ILs reduces the crystallinity and glass transition temperature of the polymeric matrix, thus improving Li^+ transport and conductivity, stabilising the electrode-SPE interfacial contact, and allowing for easier Li^+ removal and plating during the charge–discharge process.[20] Among ILs, imidazole-based ILs have garnered great interest because of their several advantages, *e.g.*, high ionic conductivity, lower viscosity, and low melting point.[21,22] Recently, natural biomaterials have been attracting attention owing to their unique structural and physical qualities, including an abundant and renewable supply, low cost, biodegradability, biocompatibility, and non-toxicity.[23] Various biopolymers have been extensively studied, like cellulose, chitin, agar, chitosan, lignin, *etc.*,[24] where cellulose and methyl cellulose (MC) hold a special importance due to their ability to create thin films. MC contains a hydroxyl group, glycosidic and methoxy linkages for ion conduction, and transit groups that serve as hosts for Li^+ ions, resulting in good ionic conductivity.[25] PEG and methyl cellulose were chosen to be combined based on their complementary features. In general, MC contributes mechanical rigidity, while PEG provides flexibility and ion-conducting pathways through ether linkages. Their combination results in a synergistic network with enhanced toughness, reduced crystallinity, and improved ionic transport properties. The blending technique is a well-proven technique in previous literature.[26,27] However, in our previous research with the MC matrix, we found the importance of the addition of lithium salts and ionic liquids in order to increase ionic conductivity.[28] In the present work, even better results have been obtained after the introduction of PEG into the system.

Accordingly, a blended polymer electrolyte system comprising polyethylene glycol and methyl cellulose was prepared with the inclusion of dynamic aromatic disulfide moieties and imidazolium-based ionic liquids with variable anions to provide simultaneous ion transport and self-healing functions. In previous research articles, blend polymer electrolytes based on ionic liquids were mainly investigated for single ionic liquid systems without comparing the chemistry of the ions. In contrast, this work aims to compare three different anions of ionic liquids, namely $TFSI^-$, Br^-, and Ac^- and their influence on the ion transport properties and polymer dynamics. In addition, this work also introduces dynamic disulfide bonds into the polymer matrix, allowing for intrinsic self-healing through reversible covalent bond exchange. Aromatic disulfide moieties, which are not often explored for PEG/MC-based ionic liquid polymer electrolytes, were selected due to their fast exchange kinetics, and relatively low bond dissociation energy. The resulting polymer electrolyte membranes were designated as PMALT-*x*, PMALB-*x*, and PMALA-*x*, respectively, where P and M denote polyethylene glycol and methyl cellulose, A represents the aromatic disulfide moiety (2-AFD), L corresponds to the lithium salt, T/B/A indicate the anion of the ionic liquid (TFSI-, Br-, Ac-) and *x* refers to the weight percentage of lithium salt. T/B/A indicate the anion of the ionic liquid (TFSI-, Br-, Ac-) as anions and cations play a crucial role in determining ionic transport and chain mobility. In this work, we have incorporated three different anions of imidazolium-based ionic liquids. Specifically, $TFSI^-$ is a bulky, charge-delocalised and weakly co-ordinating anion. Br^- is smaller and of moderate co-ordinating strength. In contrast, acetate (Ac^-) is a highly co-ordinating anion and can interact with Li^+ strongly. The influence of polymer blending, ionic liquid chemistry, and lithium salt content on the structural, thermal, mechanical, and electrochemical properties of the membranes was systematically studied. The as-obtained self-healing solid polymer electrolytes exhibited appreciable room-temperature ionic conductivity and a stable electrochemical operating window, while retaining intrinsic self-healing behaviour. The presence of ionic liquid increases the ionic conductivity, reduces ion pairing and creates more uniform Li^+ transport, while PEG-MC provides mechanical stability as evident by the stress–strain results. Additionally, due to the presence of dynamic disulfide bonds, the electrolyte restores its original functionality after any defects. The present work provides insight into the structure–property relationship that controls ion conduction and damage tolerance (self-healing) in polymer-based electrolytes. Several comprehensive characterisation studies using XRD, SEM, DSC, TGA, and various electrochemical analyses, along with their dielectric properties, indicate their potential relevance for the design of safer and mechanically robust lithium–ion battery systems.

2. Experimental

2.1. Materials

Polyethylene glycol (PEG, Mn = 1000 g mol^{-1}) was purchased from TCI Chemicals. Methyl cellulose (>95%) (Viscosity-15cP) (degree of substitution 1-7-1.9), 2-aminophenyldisulfide (99%), 1-methylimidazole (>95%), ethyl bromide (99%), and

lithium-bis(trifluoro methanesulfonyl)cimide (LiTFSI) (99%) were all supplied by Sigma-Aldrich and kept in an argon-filled glove box prior to use. Ethyl acetate, acetonitrile, hexane, and distilled water were used as solvents and supplied by Sigma-Aldrich. To minimize moisture contamination, all reagents, including the prepared ionic liquids, were dried in a vacuum oven at 60 °C overnight prior to use.

2.2. Procedure

2.2.1. Synthesis of ionic liquid-based polymeric films. Polymeric electrolyte films were synthesised using a solvent casting approach followed by thermal treatment. To begin, 1 g each of polyethene glycol (PEG) and methyl cellulose were dissolved in 30 mL of distilled water, maintaining a 1 : 1 weight ratio. After complete dissolution, 0.5 ml of the prepared ionic liquid (refer to the SI), 1-ethyl-3-methylimidazoliumbis(trifluoromethyl sulfonyl)imide (EMIM-TFSI) and 2-aminophenyl disulfide, together with two different weight ratios (0.3 g and 0.5 g) of lithium salt, *i.e.*, 15 wt % and 25 wt%, respectively, relative to the total polymer matrix mass (PEG + MC), after preliminary optimisation to maintain a balance between ionic conductivity and mechanical integrity, were gradually introduced into the polymer solution while stirring. The mixture was then kept at 80 °C with continuous stirring for 24 hours to ensure uniform mixing in the presence of an inert atmosphere (N_2). The resulting solution was poured into a Petri dish and subjected to thermal curing at 60 °C for 24 hours, ensuring the thorough removal of the solvent and forming a transparent, self-supporting film, labelled as PMALT-*x*, where *x* denotes the weight ratio of lithium salt added. For other formulations, the same procedure was employed with the variation being the addition of different ionic liquids, such as 1-ethyl-3-methylimidazolium acetate [EMIM][Ac] and 1-ethyl-methylimidazolium bromide [EMIM][Br]. The corresponding films were denoted as PMALA-*x* and PMALB-*x*, respectively.

2.3. Characterization

2.3.1. Fundamental characterization. To understand the structure and composition of the prepared electrolytes (PMAL), spectra in the 4000–400 cm^{-1} region were scanned at 0.4 cm^{-1} resolution using a PerkinElmer C94612 Fourier transform infrared (FTIR) spectrometer. FTIR spectra were recorded using 32 scans to ensure a good signal-to-noise ratio. All measurements were performed on at least three independent samples, and average values are reported. A Bruker D8 Advance Eco was used to get the XRD analysis, which had a source at 40 kV × 25 mV and CuKα radiation. The scan range (2θ) for the XRD characterisation used was 5 to 50 with a step size of 0.01°, using Cu kα radiation with λ = 1.5406 Å. A Hitachi DSC 7020 and NEXTA STA200 (Hitachi High-Tech Science Corporation, Japan) were used to conduct differential scanning calorimetry (DSC) in the temperature range of −60 °C to 300 °C. The DSC measurements were conducted in heating–cooling–heating cycles, and the data from the second heating cycle are reported. Thermogravimetric analysis was performed in the temperature range of 25 °C to 800 °C under a nitrogen atmosphere with a heating rate of 10 °C min^{-1}. The surface morphology of the prepared electrolytes was investigated using field emission scanning electron microscopy (SEM) equipped with energy-dispersive X-ray spectroscopy (EDX) for elemental mapping. To improve conductivity and picture clarity, samples were mounted on aluminum stubs and sputter-coated with gold. SEM analysis was performed at various magnifications using accelerating voltages between 5–15 kV to reveal surface texture and structural organization. The self-healing behavior of the polymer electrolytes was studied using an optical microscope. A scratch was created on the surface of the films, and the healing process was observed over time at 60 °C for 12 h without applying any external pressure. The scratch width was measured before and after healing to evaluate the healing behavior. The healing efficiency was calculated based on the reduction in scratch width relative to the original scratch width, using the following equation.[29]

$$\eta = \frac{\text{Original scratch width} - \text{healed scractch width}}{\text{Originial scratch width}} \times 100\% \quad (1)$$

2.3.2. Electrochemical measurements. Using a Novocontrol dielectric spectrometer, the ionic conductivity of PMALs was examined between 30 °C and 100 °C. The frequency range of 0.1 Hz to 30 MHz was measured using symmetrical SS/PMAL/SS blocking electrodes.[30] The following formula was used to determine the ionic conductivity of the PMALs:

$$\sigma = \frac{L}{R \cdot S} \quad (2)$$

where *R* stands for the bulk electrolyte resistance[25] and *L* and *S* are the thickness and area of the PMAL electrolyte, respectively. Using Li/PMAL/stainless steel cells, linear sweep voltammetry (LSV) measurements were conducted at 60 °C at a scan rate of 1.0 mV s^{-1} over a potential window of 0–7.0 V *versus* Li^+/Li to determine the electrochemical stability window of the PMAL electrolytes. All measurements were analyzed using NOVA 1.11.2 software (Metrohm Autolab). Furthermore, electrochemical impedance spectroscopy (EIS) was performed at 60 °C using a symmetric Li/PMAL/Li configuration to evaluate the interfacial resistance between the self-healing solid polymer electrolyte (SHSPE) membrane and lithium metal electrodes. The frequency range was examined from 100 kHz to 1 Hz with an amplitude of 10 mV.[31] The activation energy of ion transport was obtained by using the temperature dependence of the ionic conductivity that was measured by EIS. The ionic conductivity, σ, was measured in the selected temperature range and the respective temperatures were converted into absolute temperature, *T* (K). The activation energy, E_a, was determined using the Arrhenius relationship:[32]

$$\sigma = \sigma_0 \cdot \exp\left(-\frac{E_a}{kT}\right) \quad (3)$$

where σ_0 is the pre-exponential factor and *k* is the Boltzmann constant (8.617×10^{-5} eV K^{-1}). Linear fitting of ln(σ) as a

function of inverse temperature ($1/T$) was done, from which E_a was obtained from the slope in accordance with the slope ($= -E_a/k$). The lithium–ion transference number (t_{Li^+}) of PMALT was evaluated by potentiostatic polarization using symmetric Li/PMAL/Li cells at 60 °C. A constant DC potential of 4 V was applied to the cell until a steady-state current was attained. The value of t_{Li^+} was subsequently calculated using the equation given below:[33]

$$t_{Li^+} = \frac{I_s(\Delta V - I_0 R_0)}{I_0(\Delta V - I_s R_s)} \quad (4)$$

where ΔV is the applied voltage, I_0 and I_s are the initial and steady-state currents, and R_0 and R_s refer to the corresponding initial and steady-state resistances. All of the electrochemical measurements were conducted in an argon-filled glove box (<0.5 ppm H_2O/O_2).

3. Results and discussion

3.1. Fundamental properties of self-healable electrolytes

PMALT-x%, PMALB-x%, and PMALA-x% consisting of PEG, MC, and 2-AFD, $LiClO_4$, and ionic liquids (EMIM-Br, TFSI, Ac) were prepared using a simple solvent casting method. Initially, ionic liquids were successfully prepared through an anion exchange reaction of EMIM-Br with Li-TFSI and K-Ac, where the structure was investigated by ATR-FTIR and NMR spectroscopy (Figure S1 and S2). ATR-FTIR analysis was also performed for the characterization of the prepared blend electrolytes as displayed in Fig. 1(b), where a broad O–H stretching band

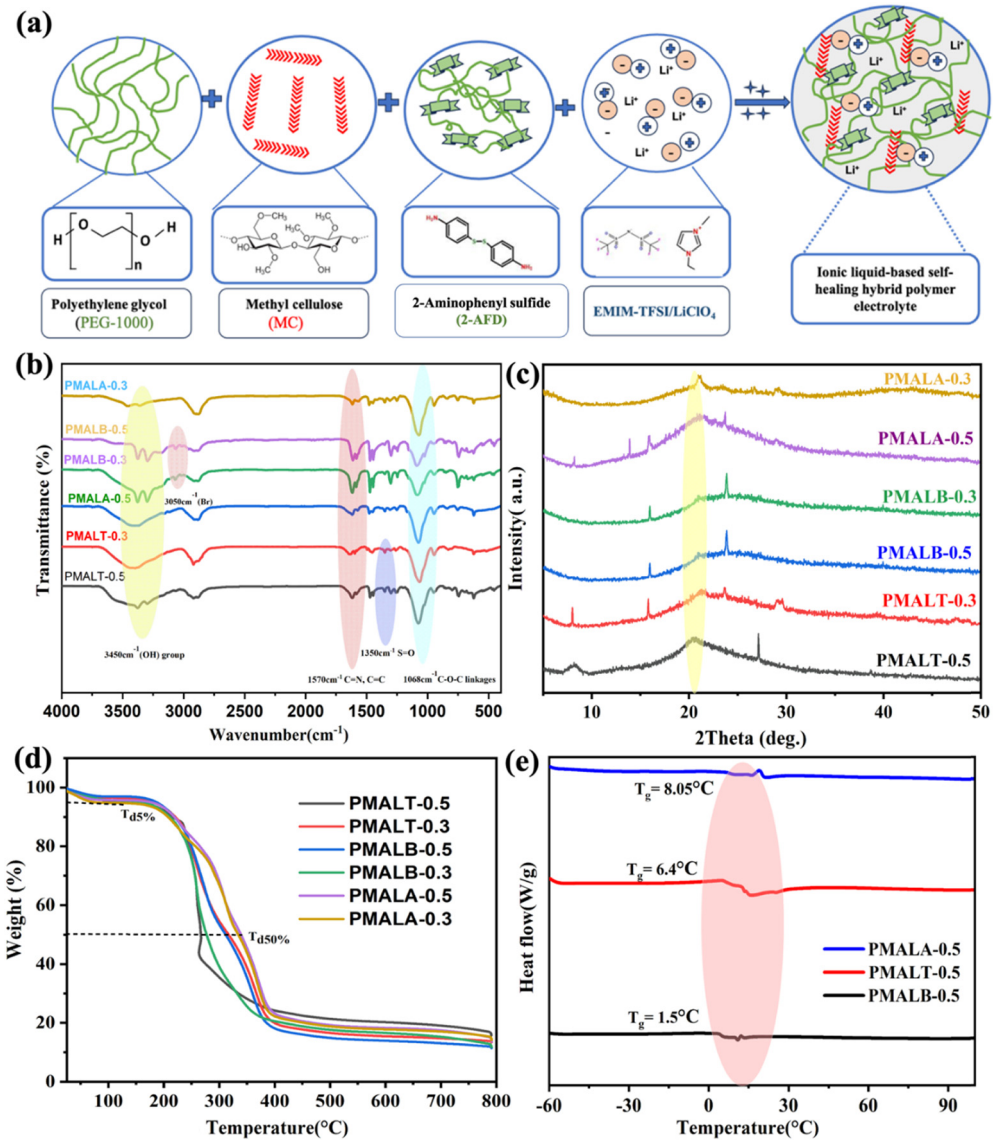

Fig. 1 (a) Schematic diagram of the preparation of self-healable ionic liquid-based polymer electrolytes, (b) ATR-FTIR spectra of the prepared electrolytes, (c) X-ray diffraction pattern (XRD) of the prepared electrolytes, (d) thermogravimetric analysis (TGA) of the electrolytes, and (e) differential scanning calorimetry (DSC) thermograms of PMALB-0.5, PMALT-0.5 and PMALA-0.5%.

located at around 3450 cm^{-1} is attributed to hydroxyl groups of both PEG and methyl cellulose, indicating extensive hydrogen bond formation within the polymer matrix involving PEG, MC, Li^+, 2-AFD, and ionic liquids. The C–O–C symmetric stretching band of the PEG backbone appears at ~1068 cm^{-1}. Additionally, the C–O stretching vibration of the pyranose ring from methyl cellulose is observed at ~1020–1070 cm^{-1}.[34] A characteristic S–S stretching vibration around ~500–550 cm^{-1} confirms the presence and integrity of the disulfide bonds in the 2-AFD structure, as designed/required for incorporating the self-healing properties. For the different ionic liquids, the observation of a band at ~3050 cm^{-1} in the EMIM-Br, TFSI, and Ac samples demonstrates the existence of C–N stretching at about 1170 cm^{-1} and aromatic C–H stretching of the imidazolium cation. The imidazole ring's C═C and C═N stretching vibrations are detected at 1634 cm^{-1} and 1570 cm^{-1}, respectively. Additionally, the TFSI anion bands present at 1350 cm^{-1} (S═O stretch), 740–750 cm^{-1}, and 1050–1100 cm^{-1} correspond to various CF_3 and S–N–S modes, confirming the presence of TFSI.[35] For EMIM-Ac, the replacement of Ac is confirmed by the strong and broad absorption bands at 1597 and 1338 cm^{-1}.[26] To confirm the crystallinity of the prepared electrolytes, X-ray diffraction was performed as shown in Fig. 1(c), where all of the samples show broad humps located at ~19°–21°, corresponding to the amorphous phase of PEG and methyl cellulose. The absence of any sharp peaks validates good dispersion of the Li-salt and ionic liquids, and their highly disordered and amorphous nature, essentially important for ionic conductivity. The values of degree of crystallinity (%) for all the samples were calculated using equation ES-1. Although PMALT samples showed broad amorphous features, weak, narrow crystalline peaks emerged at ~9°, 18° and 28°, whereas PMALB samples showed little crystalline peaks emerging at ~21° and 23°, and PMALA samples showed multiple sharp peaks across ~9°, 18°, 20° and 23° due to crystalline lattice formation, suggesting a phase separation or crystallization of EMIM-Ac, owing to Li–Ac crystallisation formation. As observed from the graph, a high concentration of lithium salt leads to poor dispersion and causes the formation of microcrystalline domains. The values of crystallinity follow the order-PMALA 0.5 (24.26%) > PMALT 0.5 (24%) > PMALA 0.3 (22.3) > PMALT 0.3 (19%) > PMALB 0.3 (18%) > PMALB 0.5 (17.35).

3.2. Thermal properties

To investigate the thermal stability of the prepared polymeric electrolytes, thermogravimetric analysis (TGA) was performed from 25 °C to 800 °C as depicted in Fig. 1(d). All the prepared samples reveal a two-step degradation pattern, where a minor weight loss below 100 °C occurred due to the evaporation of trapped moisture. All the prepared samples exhibit major degradation at around 250–300 °C, which is due to the decomposition of cellulose, and at around 350 °C corresponding to the degradation of polyethylene glycol.[23] Accordingly, these values are comparable to those of several reported polymer electrolytes, which generally show stability until 250–300 °C.[36] Notably, the degradation onset temperature was observed in the order of PMALA > PMALB > PMALT, indicating that the PMALA-based electrolytes exhibit the highest thermal stability, while the TFSI-anion based systems exhibit an earlier decomposition. This might be due to the bulky and flexible anion of $TFSI^-$, which induces the mobility of the polymer chains and loosens the cohesive energy of the network.[37] In contrast, the smaller and more coordinating acetate anion strengthens the hydrogen bonding inside the polymer-IL framework, thus the composition demonstrates higher stability. To investigate phase transitions, crystallinity, and segmental mobility in the polymer-based electrolytes, DSC analysis was performed, Fig. 1(e). The glass transition temperature (T_g) provides insight into the polymer chain flexibility.[38]

Reduced T_g enhances segmental mobility, thereby promoting lithium–ion hopping and improving electrode–electrolyte interfacial contact.[39] The T_g results perfectly validate the XRD and ionic conductivity data, where XRD results support that the PMALA sample demonstrates the highest crystallinity and highest T_g (8.05 °C) with the lowest ionic conductivity (6.8×10^{-5} S cm^{-1}), whereas PMALB shows the lowest T_g of 1.5 °C and highest ionic conductivity (8.2×10^{-4} S cm^{-1}), and PMALT shows a T_g of 6.4 °C and moderate ionic conductivity. To analyse the surface morphology, FE-SEM was performed. As can be observed from the SEM image in Fig. 2(a) of PMALT-0.5, no obvious cracks were observed on the specimen surface, indicating a well-formed polymer/ionic liquid network with smooth morphology.

The EDS spectrum in Fig. 2(b) confirms the presence of C, O, N, F, and S, consistent with the PEG-MC/IL composition, whereas elemental analysis in Fig. 2(d–f) indicates that all elements are homogeneously distributed, confirming that there is no microphase segregation between the ionic liquid and the polymer matrix.[40]

3.3. Self-healing test and dynamic properties

The mechanical strength tests were performed for the developed samples as mechanical properties play a crucial role in controlling the dendrite formation during cycling. The flexibility of the prepared samples was measured *via* stress–strain test (under flexural mode). It can also be seen that the prepared electrolytes are flexible in nature in Fig. 3(b) and (c). PMALA shows higher flexural strength along with a lower strain at break, which is consistent with its higher degree of crystallinity that restricts chain deformation under applied stress. In contrast, PMALT films exhibit greater ductility, as evidenced by a higher strain at maximum stress, reflecting the dominance of amorphous regions that allow enhanced chain mobility. The PMALB sample demonstrates intermediate mechanical behaviour, corresponding to a balanced crystalline–amorphous structure that provides moderate strength and appreciable extensibility. Overall, the stress–strain response across the series reflects a trade-off between rigidity and ductility governed by variations in crystallinity. For investigating the self-healing ability of the prepared samples, a simple scratch recovery test was carried out using optical microscopy, which has been used as an efficient technique to observe the self-healing mechanism in vitrimers.[41,42] It allows for observation

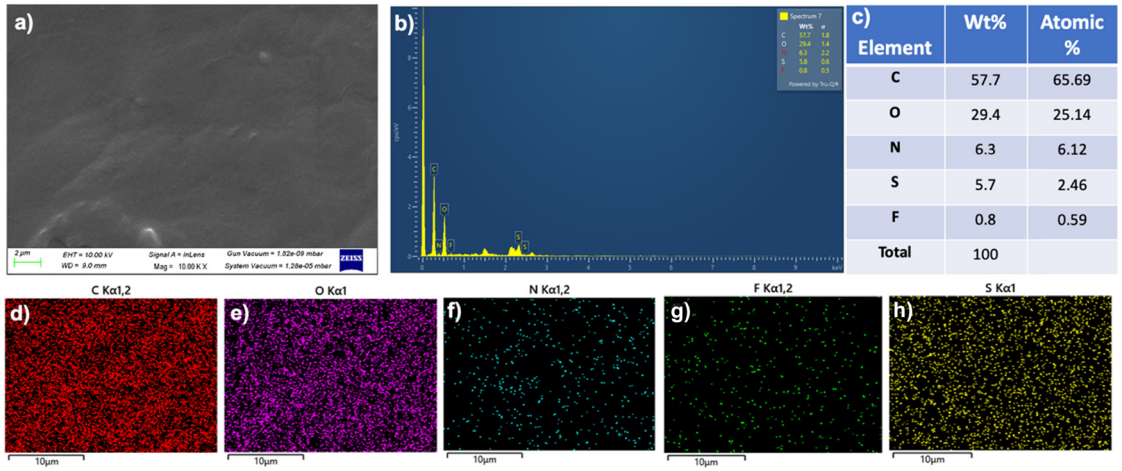

Fig. 2 (a) SEM Image of PMALT-0.5, (b) EDX analysis, (c) table of EDX element wt%, and (d)–(h) the corresponding elemental analysis of the C, O, N, F and S elements.

of the direct visualization of crack closure and interfacial healing, highly relevant to battery applications where micro-cracks and voids govern ionic transport. The electrolyte surface was scratched using a sharp blade and then the healing of the scratch was observed at different healing times. The test was repeated on three independently prepared samples to ensure reproducibility, and consistent healing behaviour was observed in all cases. Initially, the width of the crack was found to be 0.310 μm (Fig. 3(d)), which indicates the mechanical rupture of polymeric bonds. Later, the sample was exposed to mild thermal treatment at 60 °C and after 3 h of exposure time, there was a significant reduction in the width of the crack to 0.159 μm (Fig. 3(e)), which reveals the partial rearrangement of the polymeric network. Upon extending the time to 12 h the crack width reduced significantly to 0.077 μm (Fig. 3(f)), demonstrating a recovery up-to 75%. To calculate the healing efficiency of our self-healable electrolyte, eqn (1) was used. The healing was further validated by performing multiple cycles on the same sample, where consistent scratch healing efficiency was observed in each cycle, which indicates the reproducible self-healing capability of the prepared electrolyte (Fig. S4). The self-healing is because of the presence of dynamic disulfide reversible metathesis of 2-AFD, incorporated in the polymeric network. Also, the presence of an ionic liquid accelerates the healing process due to the formation of hydrogen bonding between the imidazole ring in EMIM and the ether oxygen of PEG.[43]

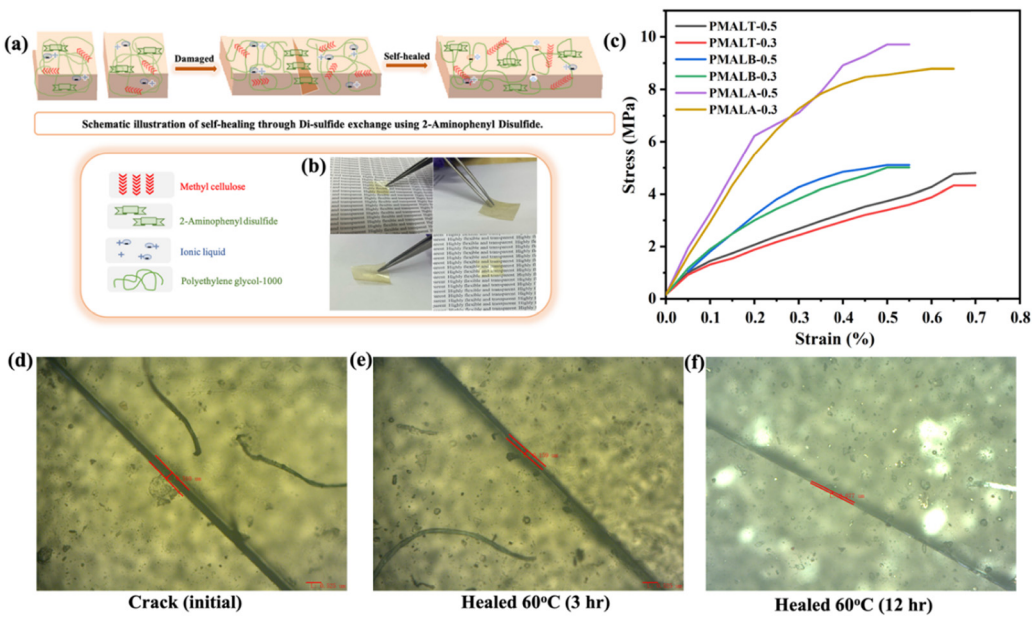

Fig. 3 (a) Illustration of self-healing through disulfide exchange, (b) images of the prepared flexible electrolyte (PMALT-0.5), (c) stress–strain curves of the prepared electrolyte, (d) optical microscope images of the initial crack formed on the surface of the electrolyte, (e) images of the healed crack after 3 h, and (f) images of the healed crack after 12 h.

3.4. Electrochemical characterization

The temperature-dependent ionic conductivity (σ) of all of the prepared self-healable electrolytes was investigated using complex impedance spectroscopy using impedance-derived Nyquist analysis and Arrhenius plots. All samples showed σ values in the range of 10^{-5}–10^{-3} S cm^{-1}. Therefore, the present system falls well within the state-of-the-art range for solid polymer electrolytes.[32] Fig. 4(b) and (c) exhibit the Nyquist plots of PMALT-0.5 and PMALB-0.5, respectively, and reveal that the bulk resistance of the electrolyte decreases with a rise in temperature. Table 2 reveals that the PMALT-0.5 ionic conductivity increases from 30 °C to 100 °C reporting a maximum ionic conductivity of 1.37 × 10^{-3} S cm^{-1} (100 °C), whereas the PMALT-0.3 conductivity was found to be 2.5 × 10^{-3} S cm^{-1} (100 °C). The ionic conductivity was also calculated for samples containing bromide and acetate anions. PMALB-0.5 shows the highest ionic conductivity of 9.15 × 10^{-3} S cm^{-1} (100 °C), whereas PMALB-0.3 shows comparable values of 4.5 × 10^{-3} S cm^{-1} (100 °C). It is noteworthy that the samples containing EMIM–Br ionic liquid show the highest conductivity, followed by EMIM–TFSI and then EMIM–Ac. This trend is in excellent agreement with the changes in glass transition temperature (T_g) and activation energy (E_a), which increase in accordance with the degree of crystallinity. It is interesting to mention here that ionic conductivity shows an inverse trend; *i.e.*, the highest ionic conductivity is observed for the least crystalline sample, *i.e.*, PMALB-0.5, and the lowest ionic conductivity is observed for the most crystalline sample, *i.e.*, PMALA-0.5. Thus, the combined analysis of X_c, T_g, E_a, and ionic conductivity provides strong and consistent evidence that increased crystallinity enhances rigidity while simultaneously hindering ion transport. The combined table containing all values is attached in the SI (Table S1), whereas the bulky weakly coordinating TFSI$^-$ anion usually facilitates higher ion mobility.[44] This might be due to the combined contribution of charge carrier concentration, strength of ion dissociation and the effects of polymer–ion interaction. The smaller Br$^-$ anion exhibits higher dielectric interaction with the polymer matrix, which favours Li$^+$/anion dissociation and results in a larger population of mobile charge carriers. As a result, for EMIM–TFSI samples, a higher fraction of Li$^+$ remains associated either with the polymer backbone or as part of transient ion pairs, reducing the number of free ions contributing to σ. Among all the samples containing an acetate anion, PMALA-0.5 exhibited the least ionic conductivity. The acetate anion is highly coordinating and capable of strong hydrogen-bonding, which promotes polymer–anion association and enhances local structural ordering. Fig. 4(a) depicts the Arrhenius plot of the developed electrolytes and the graph reveals that the ionic conductivity of all the electrolytes progressively increases with an increase in temperature from 30 °C to 100 °C. The activation energy (E_a) was determined using eqn (3) based on the Arrhenius analysis, and the calculated values are presented in Table 1, where the PMALB-based sample shows the lowest activation energy value of 0.33 eV. The calculated value of activation energy is 0.33 eV and it is a characteristic of segmental-motion-assisted rather than pure hopping mechanism.

To gain further insights into the ion conduction mechanism, complex impedance spectroscopy was carried out over a wide range of temperatures and frequencies. Fig. 5(a) displays the variation of the real dielectric component (ε') of the prepared self-healable polymer electrolyte (PMALT-0.5) with

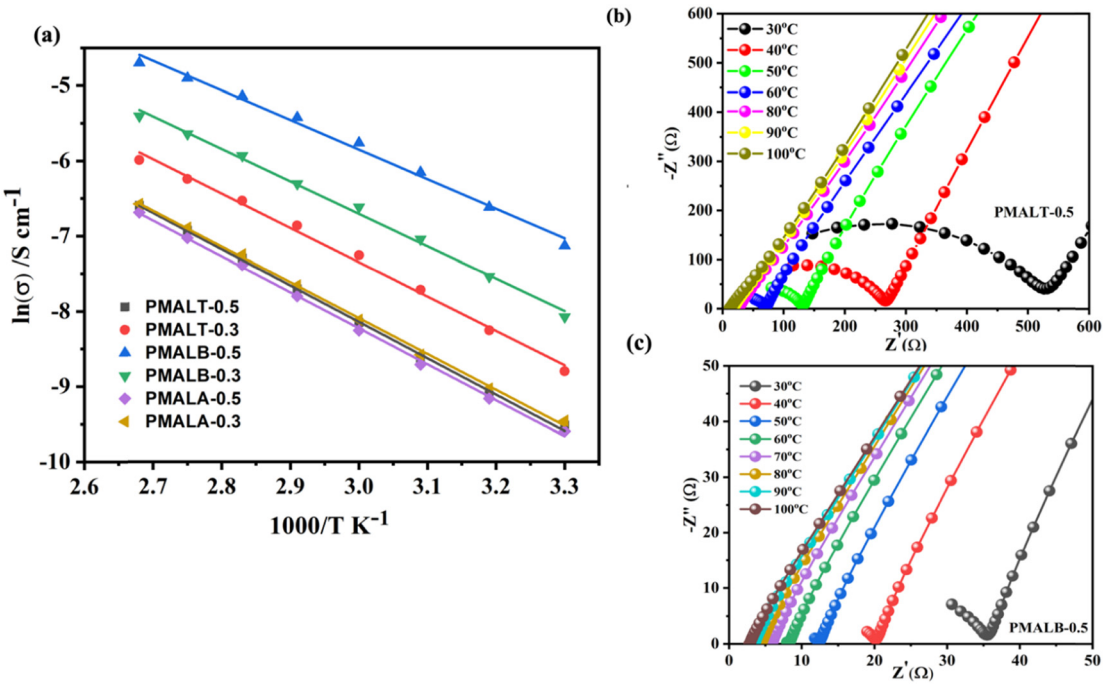

Fig. 4 (a) Arrhenius plot for the blend polymer electrolytes, and temperature dependent Nyquist plots for (b) PMALT-0.5 and (c) PMALB-0.5 s.

Table 1 Calculated activation energy (kJ mol^{-1} and eV) for the series of self-healable blend polymer electrolytes

S. no.	Sample name	Activation energy (kJ mol^{-1})	Activation energy (eV)
1	PMALT-0.5	39.41	0.41
2	PMALT-0.3	37.97	0.39
3	PMALB-0.5	32.68	0.33
4	PMALB-0.3	35.98	0.37
5	PMALA-0.5	39.73	0.41
6	PMALA-0.3	39.51	0.42

frequency. It is evident from the graph that the value of (ε') decreases with an increase in the frequency. This is due to the fact that at low frequency, these ions have enough time to migrate and accumulate at the electrode–electrolyte interface, thus providing large polarisation and hence a higher value of (ε').[45] In contrast, at higher frequency, the electric field fluctuates very fast; therefore, ions cannot follow the field and consequently the polarisation drops leading to a lower value of (ε'). Additionally, (ε') increases with increase in temperature as at higher temperature the ionic mobility increases the dipolar polarisation and thus weakens the intermolecular forces, where the ionic and electronic component contribute more to the polarisation at higher temperature.[46] The same trend of polarisation can also be observed in the imaginary dielectric constant *vs.* frequency plot. Fig. 5(b) represents that dielectric loss arises from the movement of charge carriers and energy dissipation during polarisation.[47] The increase in (ε'') with temperature is due to the activation of energy carriers in the presence of heat. Fig. 5(c) and (d) display the real (σ') and imaginary parts of the conductivity (σ'') *vs.* frequency, where a three-region profile of ionic conductivity of the polymer electrolyte appears. Electrode polarisation and limited long range ion mobility keep the real part of the complex conductivity essentially constant in the low frequency region. At intermediate frequencies, there is a rapid rise in σ', indicating the commencement of ion hopping and the breakdown of interfacial polarization. At higher frequencies, σ' approaches a second plateau, indicating charge carrier hopping across small distances and confined areas.[48] Conductivity rises progressively with temperature from 30 to 100 °C, reflecting greater segmental mobility of the PEG-MC matrix, better ion dissociation from the ionic liquid and salt, and lower system viscosity. This temperature-activated behavior is consistent with Jonscher's universal power law and indicates that polymer segmental dynamics and hopping drive ionic mobility in the electrolyte.[49] On the other hand, the imaginary part of the conductivity (σ'') exhibits a continuous increase in the value of σ'' with an increase in frequency, which is observed in various polymer systems consisting of strong ion dynamics. In the low-frequency region, the results due to the polarisation effects originated from the delayed response of charge carriers to the applied field. Beyond f_{on}, σ'' increases with an increase in frequency and reaches a maximum at f_{max}, corresponding to a condition for maximum electrode polarization. At still higher frequencies, σ'' continues to increase because of the increased contribution from localized ion hopping and fast dipolar relaxation. It is important to note that with increasing temperature, both f_{on} and f_{max} shift to higher frequencies, confirming thereby that the thermal energy enhances charge-carrier mobility, accelerates polarization relaxation, and facilitates faster hopping in the polymer matrix.[30] Fig. 5(e) represents a σ'-frequency plot of PMALT-0.5, which reflects a well-defined DC plateau at low frequencies due to stable long-range ionic motion. With the increase in frequency, σ' increases gradually, followed by a sharp rise, indicating transition into the hopping/segmental-relaxation regime that corresponds to localized rapid motions of ions. The nature of this dispersion indicates that an efficient ion-transport pathway does exist within the PEG-MC-ionic liquid hybrid matrix. The relationship between the loss tangent *vs.* frequency and the plot of the imaginary part of the conductivity is shown in Fig. 5(f). It is evident that the loss tangent plot's maximum coincides with the minimum associated with the onset polarization.[47]

For validating the practical use of the prepared electrolyte in solid-state batteries, we have further investigated its electrochemical stability window (ESW), as it is essential that the electrolyte must not undergo any oxidation or decomposition in the charge–discharge range of the batteries (*i.e.*, up to 4 V for typical Li-based batteries). ESW is measured by linear sweep voltammetry from 1 V to 7 V at 60 °C.[41,50] Indeed, among all the different compositions, PMALT-0.5 shows the widest electrochemical stability window, portraying an oxidative current onset at around 5.8–6.0 V *vs.* Li^+/Li as shown in Fig. 6(a). This obviously suggests that the higher salt concentration in PMALT-0.5 improves the structural integrity of the polymer–ionic liquid network, with suppression of premature oxidation. By comparison, PMALT-0.3 exhibits a much lower oxidative limit of ~4.5 V as depicted in Fig. 6(b), reflecting that insufficient lithium–ion-coordination and the weaker ionic crosslinking

Table 2 Calculated values of temperature-dependent ionic conductivity for the series of blend polymer electrolytes

Temperature	PMALT-0.5	PMALT-0.3	PMALB-0.5	PMALB-0.3	PMALA-0.5	PMALA-0.3
30 °C	7.37×10^{-5}	1.51×10^{-4}	8.02×10^{-4}	3.11×10^{-4}	6.80×10^{-5}	7.82×10^{-5}
40 °C	1.10×10^{-4}	2.60×10^{-4}	1.34×10^{-3}	5.31×10^{-4}	1.05×10^{-4}	1.20×10^{-4}
50 °C	1.79×10^{-4}	4.46×10^{-4}	2.13×10^{-3}	8.76×10^{-4}	1.65×10^{-4}	1.88×10^{-4}
60 °C	2.89×10^{-4}	7.07×10^{-4}	3.16×10^{-3}	1.34×10^{-3}	2.60×10^{-4}	2.99×10^{-4}
70 °C	4.51×10^{-4}	1.05×10^{-3}	4.41×10^{-3}	1.83×10^{-3}	4.10×10^{-4}	4.73×10^{-4}
80 °C	6.80×10^{-4}	1.46×10^{-3}	5.87×10^{-3}	2.66×10^{-3}	6.20×10^{-4}	7.15×10^{-4}
90 °C	9.85×10^{-4}	1.95×10^{-3}	7.45×10^{-3}	3.55×10^{-3}	8.90×10^{-4}	1.02×10^{-4}
100 °C	1.37×10^{-3}	2.51×10^{-3}	9.13×10^{-3}	4.50×10^{-3}	1.25×10^{-3}	1.40×10^{-3}

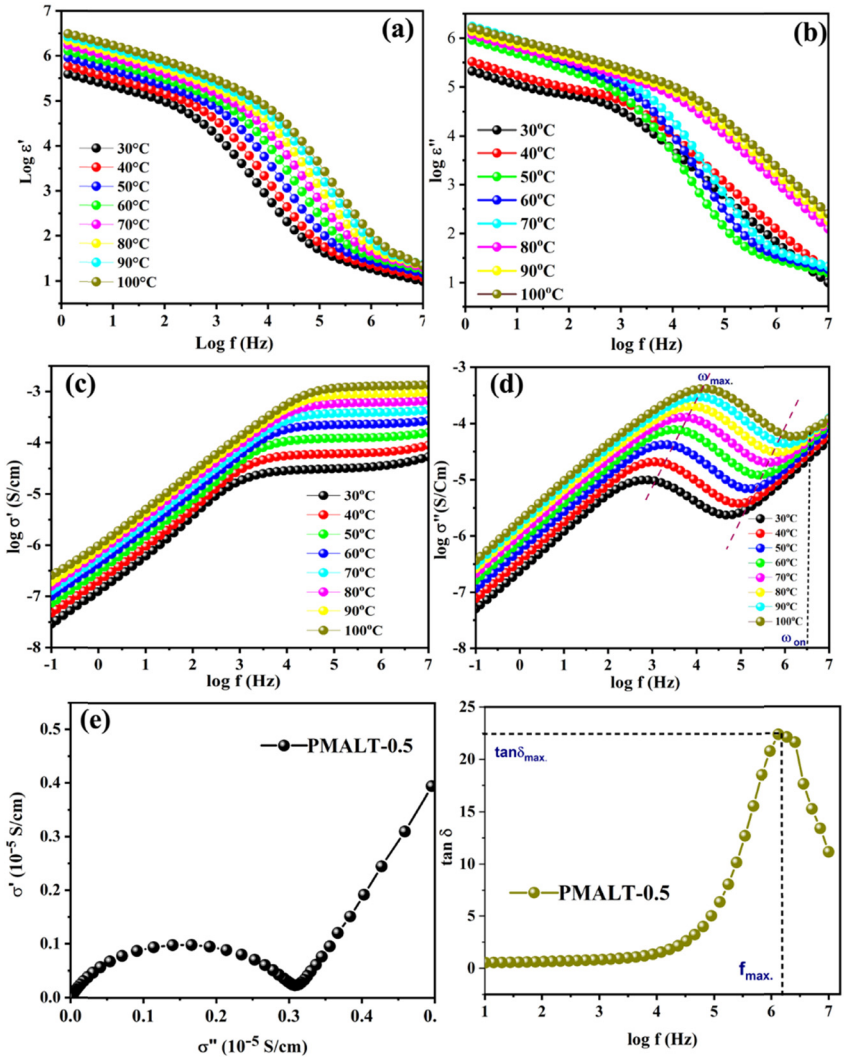

Fig. 5 (a) Frequency dependent real (ε') and (b) imaginary part of the dielectric constant, (c) real and (d) imaginary conductivity plot from 30 °C to 100 °C of PMALT-0.5, (e) plot between the real part of the conductivity and imaginary conductivity of PMALT-0.5, and (f) relationship between loss tangent (tan δ) and frequency.

produce a more labile interfacial environment. As such, the electrolyte decomposes at much lower potentials. The reason for the increased conductivity of PMALT-0.3 is due to the optimized balance of ion concentration and mobility of the polymer chains, whereas increased salt concentration in PMALT-0.5 resulted in ion agglomeration and decreased mobility, causing decreased conductivity. On the other hand, increased salt concentration enhances electrochemical stability due to a more stable environment for ions and inhibits oxidation reactions. Interestingly, while the bromide-based samples (PMALB) and acetate-based samples (PMALA) provide the highest and least ionic conductivity, respectively, their oxidative stability was not wide enough, with decomposition occurring well below 4 V. This observation confirms that ionic conductivity does not directly correlate with electrochemical stability. High conductivity may arise from enhanced ion mobility or weaker polymer–ion interactions, but these same features often reduce the resistance of the polymer backbone and ionic liquid anion toward oxidative degradation. Thus, according to the ESW results, only the TFSI-based PMALT series meets the stability criteria to proceed with the electrochemical testing presented in this work. Its superior electrochemical durability will make PMALT-0.5/0.3 a more reliable candidate to assemble full cells and study long-term cycling. Apart from ionic conductivity and decomposition voltage, lithium–ion transference is also crucial for evaluating solid-state electrolytes' electrochemical performance. As a lower lithium–ion transference number increases the electrode polarisation and reduce the battery performance.[27] Using the Li/PMALs/Li symmetric cells at 60 °C, the lithium–ion transference number (t_{Li^+}) of PMALT was calculated using the potentiostatic polarization method. A stable solid electrolyte interphase (SEI) layer was successfully formed on the electrode surface by polarizing the symmetric cell with a voltage of 0.4 V until the current reached the steady state. The overall resistance of the cell (Li/PMALT-0.5/Li) before and after polarisation was measured by electrochemical impedance spectroscopy as shown in Fig. 6(c) and (d). The values were then used in eqn (4) to calculate the

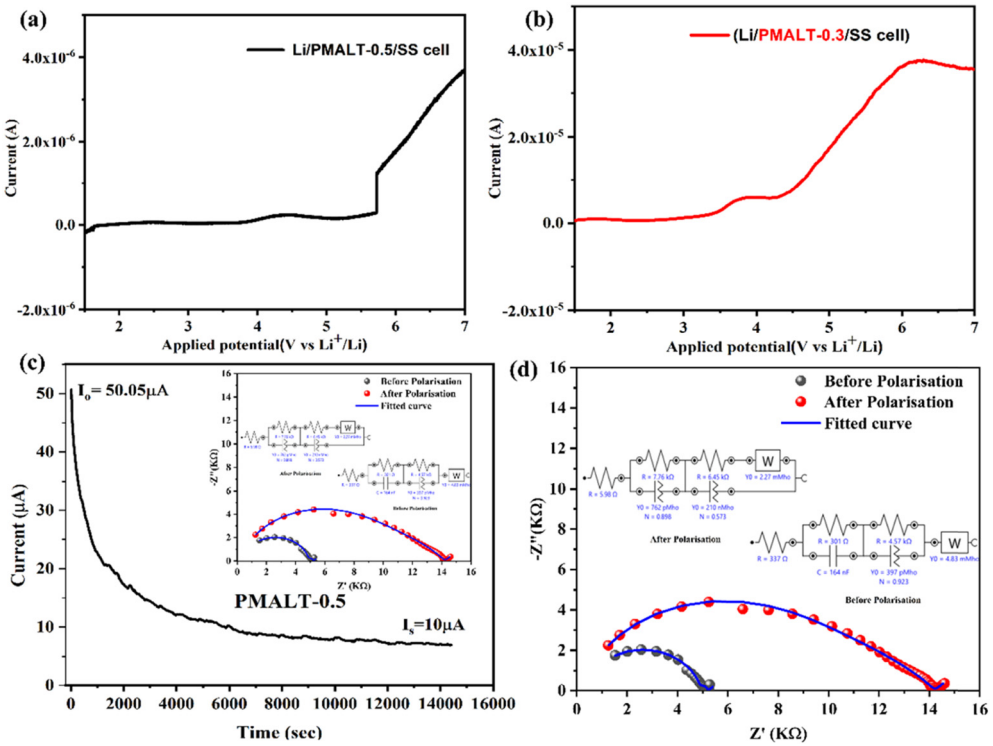

Fig. 6 (a) Linear sweep voltammetry (LSV) of Li/PMALT-0.5/SS cell at 60 °C, (b) LSV of Li/PMALT-0.3/SS cell at 60 °C, (c) chronoamperometry profile of Li/PMALT-0.5/Li at 60 °C, (d) electrochemical impedance spectroscopy (EIS) of PMALT-0.5/SS before and after polarisation.

Li-transference number. Here, we have found that the transference number of PMALT-0.5 is 0.12–0.13. The values are comparable to the published literature related to the ionic liquid-based PEO electrolytes[51]

4. Conclusion

In conclusion, a class of self-healable polymer electrolytes based on ionic liquids was successfully prepared and investigated for solid-state lithium–ion batteries. To the best of our knowledge, this study is among the first to report the simultaneous realization of electrochemical performance and self-healing capability by the incorporation of three different ionic liquid comparisons into a PEG/MC/2-AFD polymer matrix. The formation of a strongly interacting yet dynamically reversible polymer–ion network was established by thorough spectroscopic and physicochemical characterisation. While XRD showed a predominantly amorphous structure confirming enhancement in the free volume for rapid ion transport, the FTIR spectra demonstrated molecular-level interactions of the ionic liquid with the polymer chains and Li^+. With a T_g of 1 °C, DSC further supported this structural flexibility, showing improved conductivity. For battery applications, TGA revealed excellent thermal stability until 300 °C, ensuring its safe operation. The mechanical robustness of the electrolytes without sacrificing flexibility, a key prerequisite for reliable electrode–electrolyte interfacial contact, was evidenced by mechanical testing showing the stress and strain relationship. For application as a battery electrolyte, ionic conductivity, electrochemical stability window (ESW), and lithium–ion transference number are crucial parameters. Ionic conductivity was evaluated using complex impedance spectroscopy, giving the highest value of conductivity of 9.13×10^{-3} at ambient temperature. The electrochemical stability window was evaluated using a Li/PMAL/SS cell, revealing a wide stability range of approximately 5.8–6.0 V. Furthermore, the lithium–ion transference number was calculated using the Bruce–Vincent equation to assess the contribution of mobile Li^+ ions, yielding values of 0.12–0.13 for the polymer electrolyte. The electrochemical analysis revealed clear distinctions between the anion variations. The bromide-based electrolyte has the maximum ionic conductivity among the produced compositions due to the stronger ion dissociation. However, the TFSI-based sample significantly outperformed all others in the properties most critical to solid-state battery operation. Specifically, the $TFSI^-$ system delivered the widest electrochemical stability window, the highest Ls^+ transference number, superior healing efficiency, and mechanical durability under stress and ionic conductivity values (10^{-4}–10^{-3} S cm^{-1}). These attributes, together with the fast ion transport supported by the high amorphous content and low T_g, establish that high conductivity alone is not the determining parameter. Hence, it is an excellent candidate for next generation self-healable solid state batteries.

Author contributions

K. A. conceptualization, methodology, investigation, data curation, formal analysis, visualization, and writing – original draft.

S. P. S. investigation, resources, formal analysis, and writing – review & editing. P. J. investigation, validation, and writing – review & editing. M. S. L. resources, validation, and writing – review & editing. R. S. resources, supervision, and writing – review & editing. S. R. supervision, conceptualization, methodology, project administration, and writing – review & editing.

Conflicts of interest

There are no conflicts to declare.

Data availability

Supplementary information (SI) is available. See DOI: https://doi.org/10.1039/d6ma00073h.

Acknowledgements

Kaushiki Ahuja would like to acknowledge UPES for the JRF fellowship and UPES-CIC for the instrumental support and facilities. The authors sincerely acknowledge Banaras Hindu University for access to electrochemical characterisation facilities. The authors gratefully acknowledge the financial support provided by the National Mission on Himalayan studies (NMHS) under Ref. No. NMHS/2022-23/MG86/03/279 and NMHS2024-25/SC-XIII/SG/SL-32.

References

1 J. Kalhoff, G. G. Eshetu, D. Bresser and S. Passerini, *ChemSusChem*, 2015, **8**, 2154–2175.
2 A. Rajkamal and R. Thapa, *Adv. Mater. Technol.*, 2019, **4**, 1900307.
3 T. Chen, W. Kong, Z. Zhang, L. Wang, Y. Hu, G. Zhu, R. Chen, L. Ma, W. Yan, Y. Wang, J. Liu and Z. Jin, *Nano Energy*, 2018, **54**, 17–25.
4 B. Fang, R. Wang, H. Liang and R. Mo, *J. Mater. Sci. Technol.*, 2026, **245**, 256–265.
5 X. Tian, P. Yang, Y. Yi, P. Liu, T. Wang, C. Shu, L. Qu, W. Tang, Y. Zhang, M. Li and B. Yang, *J. Power Sources*, 2020, **450**, 227629.
6 H. Gan, Y. Zhang, S. Li, L. Yu, J. Wang and Z. Xue, *ACS Appl. Energy Mater.*, 2021, **4**, 482–491.
7 Z. Katcharava, A. Marinow and W. H. Binder, *Royal Society of Chemistry*, 2025, preprint, DOI: 10.1039/d4cc05428h.
8 K. Ahuja, P. Singh, N. Banerjee, S. Rana, G. J. Yun, F. Ahmad and M. Jamil, *Elsevier Ltd*, 2025, preprint, DOI: 10.1016/j.est.2025.117077.
9 X. Ming, J. Du, C. Zhang, M. Zhou, G. Cheng, H. Zhu, Q. Zhang and S. Zhu, *ACS Appl. Mater. Interfaces*, 2021, **13**, 41140–41148.
10 L. Gao, W. Jiang, X. Zhang, Y. Sun, K. Chen, W. Li, H. Xie and J. Liu, *Chem. Eng. J.*, 2024, **479**, 147822.
11 H. Kuang, H. Liao, Z. Zhang, S. Huang, B. Mao, W. Shan, X. Duan, X. Feng and T. Li, *J. Colloid Interface Sci.*, 2026, **707**, 139638.
12 Y. Song, Y. Jiang, L. Deng and G. Yang, *Chem. – Eur. J.*, 2022, **28**, e202202717.
13 P. Halsi, P. Singh, A. Rana, M. Singh, N. G. Sahoo, S. Rana and R. Patel, *Polym. Compos.*, 2026, **47**, 5928–5942.
14 B. Krishnakumar, R. V. S. P. Sanka, W. H. Binder, V. Parthasarthy, S. Rana and N. Karak, *Chem. Eng. J.*, 2020, **385**, 123820.
15 F. Herbst, D. Döhler, P. Michael and W. H. Binder, *Macromol. Rapid Commun.*, 2013, **34**, 203–220.
16 B. Zhou, Y. H. Jo, R. Wang, D. He, X. Zhou, X. Xie and Z. Xue, *J. Mater. Chem. A*, 2019, **7**, 10354–10362.
17 Z. Katcharava, T. E. Orlamünde, L. T. Tema, H. Hong, M. Beiner, B. Iliev, A. Marinow and W. H. Binder, *Adv. Funct. Mater.*, 2024, **34**, 2403487.
18 I. Raguž, M. Berer, C. Holzer, B. Vanderborght, J. Brancart and S. Schlögl, *J. Appl. Polym. Sci.*, 2025, **143**, e58024.
19 B. Zhou, M. Yang, C. Zuo, G. Chen, D. He, X. Zhou, C. Liu, X. Xie and Z. Xue, *ACS Macro Lett.*, 2020, **9**, 525–532.
20 N. A. Noorhisham, D. Amri, A. H. Mohamed, N. Yahaya, N. M. Ahmad, S. Mohamad, S. Kamaruzaman and H. Osman, *J. Mol. Liq.*, 2021, **326**, 115340.
21 S. P. Singh, E. Masiewicz, R. K. Singh, S. K. Chaurasia and D. Kruk, *J. Chem. Phys.*, 2024, **161**, 174901.
22 V. Bijalwan and S. Rana, *Monatsh. Chem.*, 2025, **157**, 447–458.
23 H. Zhang, S. Wang, A. Wang, Y. Li, F. Yu and Y. Chen, *Appl. Surf. Sci.*, 2022, **593**, 153411.
24 P. Perumal, P. C. Selvin, S. Selvasekarapandian and P. Sivaraj, *Mater. Today: Proc.*, 2019, **8**, 196–202.
25 S. B. Aziz, I. Brevik, M. H. Hamsan, M. A. Brza, M. M. Nofal, A. M. Abdullah, S. Rostam, S. Al-Zangana, S. K. Muzakir and M. F. Z. Kadir, *Polymers*, 2020, **12**, 1–19.
26 S. T. C. L. Ndruru, S. Widiarto, E. Pramono, D. Wahyuningrum, B. Bundjali and I. M. Arcana, *Macromol. Chem. Phys.*, 2022, **23**, 2100362.
27 P. R. Chinnam, H. Zhang and S. L. Wunder, *Electrochim. Acta*, 2015, **170**, 191–201.
28 T. E. Jefferson, K. Ahuja, S. Mahendia, N. Banerjee and S. Rana, *Energy Storage*, 2026, **8**, e70355.
29 J. Dahlke, J. Kimmig, M. Abend, S. Zechel, J. Vitz, U. S. Schubert and M. D. Hager, *NPG Asia Mater.*, 2020, **12**, 13.
30 A. Tiwari and R. Kumar Singh, *Chem. Phys. Chem.*, 2024, **25**, e202400620.
31 A. Tiwari and R. K. Kumar Singh, *ECS Meeting Abstracts*, 2024, **MA2024-01**, 47.
32 X. Lin, S. Xu, Y. Tong, X. Liu, Z. Liu, P. Li, R. Liu, X. Feng, L. Shi and Y. Ma, *Mater. Horiz.*, 2023, **10**, 859–868.
33 X. Chen, L. Yi, J. Liu, Z. Luo, Y. Shen and X. Wang, *J. Power Sources*, 2024, **603**, 234433.
34 H. Zhang, S. Wang, A. Wang, Y. Li, F. Yu and Y. Chen, *Appl. Surf. Sci.*, 2022, **593**, 153411.
35 Y. Song, Y. Jiang, L. Deng and G. Yang, *Chem. – Eur. J.*, 2022, **28**, e202202717.

36 A. J. D'Angelo and M. J. Panzer, *Chem. Mater.*, 2019, **31**, 2913–2922.
37 J. C. Dias, D. M. Correia, C. M. Costa, G. Botelho, J. L. Vilas-Vilela and S. Lanceros-Mendez, *Polymer*, 2021, **229**, 123995.
38 W. Chen, Y. Yi, F. Hai, Z. Wu, J. Guo, X. Tian, X. Gao, W. Tang and M. Li, *Batteries*, 2023, **9**, 452.
39 C. Guo, Y. Cao, J. Li, H. Li, S. Kumar Arumugam, S. Oleksandr and F. Chen, *Appl. Energy*, 2022, **323**, 119571.
40 C. Wang, R. J. Li, P. Chen, Y. Fu, X. Y. Ma, T. Shen, B. Zhou, K. Chen, J. J. Fu, X. Bao, W. Yan and Y. Yang, *J. Mater. Chem. A*, 2021, **9**, 4758–4769.
41 B. Zhou, Y. H. Jo, R. Wang, D. He, X. Zhou, X. Xie and Z. Xue, *J. Mater. Chem. A*, 2019, **7**, 10354–10362.
42 T. Chen, W. Kong, Z. Zhang, L. Wang, Y. Hu, G. Zhu, R. Chen, L. Ma, W. Yan, Y. Wang, J. Liu and Z. Jin, *Nano Energy*, 2018, **54**, 17–25.
43 L. Gao, W. Jiang, X. Zhang, Y. Sun, K. Chen, W. Li, H. Xie and J. Liu, *Chem. Eng. J.*, 2024, **479**, 147822.
44 P. Guo, H. Zhang, X. Liu and J. Sun, *ACS Appl. Mater. Interfaces*, 2018, **10**, 2105–2113.
45 R. Dutta and A. Kumar, *J. Phys.: Conf. Ser.*, 2016, **765**, 012020.
46 A. L. Sharma and A. K. Thakur, *Ionics*, 2015, **21**, 1561–1575.
47 A. Arya, M. Sadiq and A. L. Sharma, *Mater. Today: Proc.*, 2019, **12**, 554–564.
48 A. Palui, B. Deb and A. Ghosh, *J. Appl. Phys.*, 2013, **114**, 084104.
49 A. Serghei, J. R. Sangoro and F. Kremer, *Electr. Phenom. Interfaces Biointerfaces*, 2012, 241–273.
50 T. Chen, W. Kong, Z. Zhang, L. Wang, Y. Hu, G. Zhu, R. Chen, L. Ma, W. Yan, Y. Wang, J. Liu and Z. Jin, *Nano Energy*, 2018, **54**, 17–25.
51 K. Pożyczka, M. Marzantowicz, J. R. Dygas and F. Krok, *Electrochim. Acta*, 2017, **227**, 127–135.